remote sensing

MDPI

Article

Enhanced Co-Registration Method for Long-Baseline SAR Images

Dong Zeng [1], Haiqiang Fu [1,*], Jianjun Zhu [1], Qijin Han [2], Aichun Wang [2], Mingxia Zhang [2], Kefu Wu [1], Zhiwei Liu [3,4] and Zhiwei Li [1]

[1] School of Geoscience and Info-Physics, Central South University, Changsha 410083, China; dongzeng@csu.edu.cn (D.Z.); zjj@csu.edu.cn (J.Z.); kefuwu@csu.edu.cn (K.W.); zwli@csu.edu.cn (Z.L.)
[2] China Centre for Resources Satellite Data and Application, Beijing 100094, China; hanqijin@cresda.com (Q.H.); wangaichun@cresda.com (A.W.); zhangmingxia@spacechina.com (M.Z.)
[3] School of Advanced Interdisciplinary Studies, Central South University of Forestry and Technology, Changsha 410004, China; liuzhiwei@csuft.edu.cn
[4] Institute for Computer Research (IUII), University of Alicante, 03080 Alicante, Spain
* Correspondence: haiqiangfu@csu.edu.cn

Highlights

What are the main findings?

- An enhanced fine co-registration method for long-baseline InSAR is proposed, integrating an elevation-dependent term to compensate for terrain-induced local offsets.
- Validated with China's LuTan-1 (LT-1) satellite data across two distinct test sites (Madrid, Spain; Shannan, China), the method significantly improves interferometric coherence and Digital Elevation Model (DEM) accuracy in rugged terrain.

What are the implications of the main findings?

- Addresses the inapplicability of conventional polynomial models in complex terrain under long-baseline conditions, advancing high-quality InSAR processing.
- Provides a reliable technical co-registration solution for China's LuTan-1 (LT-1) and similar long-baseline SAR satellite missions, facilitating precise topographic mapping and the development of interferometry-related applications.

Abstract

Accurate synthetic aperture radar (SAR) image co-registration is a crucial procedure for high-quality interferometry and its associated applications. Neglecting the effect of terrain elevation, conventional techniques employ simple polynomial models to achieve accurate co-registration between SAR image pairs during fine co-registration processing. However, these methods become inapplicable for tugged terrain, especially under longer spatial baseline conditions. On the basis of this, we introduced an elevation-dependent term into the conventional fine co-registration model to compensate for local offsets caused by variable topography. As a result, a new SAR image fine co-registration method was proposed. To validate the proposed method, experiments were conducted using data from China's LuTan-1 satellite in two typical study areas (Madrid, Spain, and Shannan, China), across diverse land-cover types and terrain conditions. At the Madrid test site, the proposed co-registration algorithm can effectively improve the phase quality (average coherence improves from 0.57 to 0.77), and topography accuracy (quantified by root-mean-square-error, RMSE) improved from 3.67 m to 3.59 m in mountainous regions, and it shows similar performance in relatively flat areas to that of the conventional methods. At the Shannan test site, characterized by rugged terrain, the average coherence of the interferogram

check for updates

Academic Editors: Francesca Cigna and Yasser Maghsoudi

Received: 19 November 2025
Revised: 10 December 2025
Accepted: 12 December 2025
Published: 15 December 2025

Citation: Zeng, D.; Fu, H.; Zhu, J.; Han, Q.; Wang, A.; Zhang, M.; Wu, K.; Liu, Z.; Li, Z. Enhanced Co-Registration Method for Long-Baseline SAR Images. *Remote Sens.* **2025**, *17*, 4034. https://doi.org/10.3390/rs17244034

Copyright: © 2025 by the authors. Licensee MDPI, Basel, Switzerland. This article is an open access article distributed under the terms and conditions of the Creative Commons Attribution (CC BY) license (https://creativecommons.org/licenses/by/4.0/).

obtained by our method increased from 0.32 to 0.48 compared to the conventional co-registration approach. Against the reference topographic data, the InSAR DEM retrieved by our proposed method achieved an RMSE of 6.31 m, indicating an improvement of 23%. This study provides an effective method to enhance the quality of co-registration and interferometry in areas with complex terrain.

Keywords: InSAR; co-registration; long-baseline SAR; LuTan-1; topography mapping

1. Introduction

Synthetic aperture radar interferometry (InSAR) has proven to be one of the most powerful technologies for topography mapping [1], ground deformation monitoring [2], and other applications [3–5]. SAR image co-registration is an essential procedure performed during the generation of interferograms and in applications relying on interferometric phase information, aligning the common features of SAR image pairs acquired at different dates or from different viewpoints. To meet the abovementioned applications, image co-registration is required to reach sub-pixel accuracy. For example, for the DEMs retrieved by InSAR technologies, interferogram generation requires images to be co-registered with an accuracy of better than 1/8 of a pixel to avoid significant loss of phase coherence [6].

To achieve sub-pixel co-registration accuracy, the conventional algorithms involve three stages: homonymous point selection, transformation model construction, and resampling of the slave SAR image. For homonymous point matching, the existing methods can broadly be divided into two major categories: feature-based methods [7–10] and area-based methods [11–14]. Compared to the feature-based approach, the area-based method is less affected by the quantity and spatial distribution of features in SAR images. It allows for the uniform acquisition of any number of homonymous points that are evenly distributed, and this method can significantly reduce the mismatch rate of homonymous points. Consequently, for SAR images with short revisit times, similar image geometry, and acquired by the same sensor (i.e., bistatic SAR system), the latter method is preferred.

Once a sufficient number of homonymous points between SAR image pairs are obtained, the next critical step is determining the optimal transformation model for co-registration. To achieve this goal, polynomial models have been widely used in previous studies [15,16], as well as some commercial/open-source SAR image processing software packages [17–19], owing to their simplicity and excellent approximation capabilities regarding the offset between images. By neglecting the effects of terrain and baseline length, these models perform well in regions with gentle-terrain slopes [20]. However, in scenarios with complex terrain conditions, where baseline-induced distance variations become significant, these models, which only consider planar position, become less effective in accurately depicting the transformation relationship between SAR images.

To address this issue, Yue et al. [21] proposed fitting the offset curve on a line-by-line basis. While this approach can tolerate the effects of varying terrains, determining the polynomial order is still challenging, with high-order polynomials potentially leading to the Runge phenomenon [22]. To overcome this limitation, some studies [23,24] have adopted the block-fitting method to establish the conversion relationship between SAR images. For example, Zhang et al. [23] divided the image into fixed blocks and applied the same offset to each block; however, the effectiveness of this approach relies on the consistency of the offset within each sub-block. Cheng et al. [24] applied the Getis–Ord formula to identify clusters of offsets with significant local variations. Based on the clustering results, the image was divided into multiple blocks, and a separate polynomial relationship was fitted

to the offsets in each block. However, these methods fail to account for the underlying mechanisms driving local offset generation, making it difficult to determine the optimal number, size, and shape of the blocks. Moreover, phase discontinuities are likely to occur at the boundaries between adjacent blocks.

Building on this line of investigation, our work aims to explore the effect of terrain variations on SAR image co-registration to improve topography mapping capability using long-baseline InSAR data. The focus is set on developing a more universal polynomial model to accurately represent the conversion relationship of offsets between SAR images. The core idea is to retrieve the functional relationship between terrain height and the range-direction offset based on InSAR observation geometry. Subsequently, we introduced an elevation-dependent term into the conventional fine co-registration model to compensate for local offsets stemming from variable topography. To design our experiment, we have the following specific objectives:

(i) To investigate the effect of terrain height on the co-registration of long-baseline SAR images.
(ii) To propose an enhanced model for the fine co-registration of a long-baseline InSAR pair.
(iii) To evaluate the performance of the proposed method for DEM retrieval using L-band LuTan-1 SAR data.

2. Research Background

The LuTan-1 (LT-1) satellite, launched in 2022, is China's first civilian L-band synthetic aperture radar (SAR) constellation comprising two L-band SAR satellites, LT-1A and LT-1B, which are identically designed and equipped with advanced L-band multi-polarization, multi-channel SAR payloads. To meet the needs of topographic mapping, the satellites function in a dual formation and spiral flight pattern, with intervals from 700 m to 7000 m, with a maximum spatial resolution of 3 m and a maximum observation swath of up to 400 km [25].

As elucidated in Section 1, before obtaining a high-accuracy interferometric phase, sub-pixel co-registration should be performed. Pixel offsets between the reference image point and the secondary image can be expressed as

$$\begin{cases} \Delta l = l_S - l_R \\ \Delta c = c_S - c_R \end{cases} \tag{1}$$

where the subscripts R and S denote the reference and secondary images, l refers to the row index in the azimuth direction, and c refers to the column index in the slant-range direction. The terms Δl and Δc represent the corresponding pixel offsets in the azimuth and range directions.

Assuming the SAR signal data in zero-Doppler geometry, if the trajectories of the two images used in co-registration are perfectly parallel or form only a very small angle [26], the terrain-induced azimuthal offsets can be ignored, and a conventional polynomial model can achieve effective fitting accuracy.

As shown in Figure 1, if topography with respect to an ellipsoidal reference surface is neglected, the difference between the geometric ranges from point P to satellite S_1 and to satellite S_2 can be expressed as

$$\delta R = |S_2P| - |S_1P| = R_2 - R_1 \approx -Bsin(\theta - \alpha) \tag{2}$$

where θ is the radar incidence angle, B is the total baseline length, and α is the baseline tilt angle. When topographic height is h, it causes an increase in the radar incidence angle by an increment of $\delta\theta$. In this case, the slant-range difference can be expressed as

$$\delta R^* = |S_2P^*| - |S_1P^*| = R_2^* - R_1^* \approx -Bsin(\theta + \delta\theta - \alpha) \quad (3)$$

where R_1^* and R_2^* represent the geometric range from satellites S_1 and S_2 to ground point P^*, respectively, and $\delta\theta$ denotes the incidence angle difference between the two radar antennas, which can be expressed as

$$\delta\theta \approx \frac{|PP^*|}{R_1} = \frac{h}{(R_1 sin\theta)} \quad (4)$$

Through Equations (2)–(4), the range-direction pixel offsets due to the topographic effect can be quantified as a function of terrain elevation (h), as

$$\Delta c_h = \frac{\delta R - \delta R^*}{\Delta r} \approx \frac{B_\perp}{R_1 sin\theta} \frac{h}{\Delta r} \quad (5)$$

where $B_\perp$ is the perpendicular baseline, and Δr denotes the resolution in the slant-range direction. Equation (5) reveals that the range-direction pixel offsets induced by the topographic effect are approximately directly proportional to both the perpendicular baseline and terrain elevation, while being inversely proportional to the slant range, incidence angle, and range pixel spacing. Therefore, for given terrain conditions and imaging geometry, range-direction pixel offsets scale linearly with the perpendicular baseline.

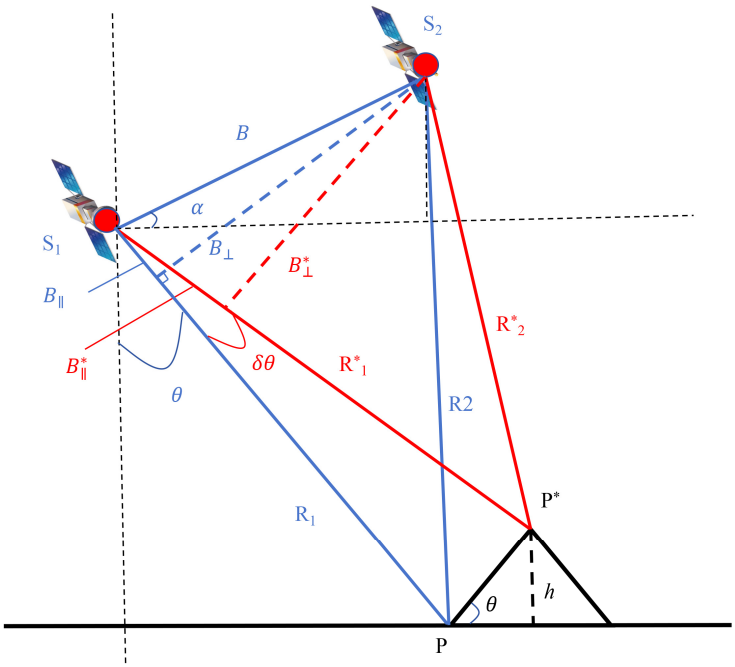


Figure 1. Range variation caused by elevation in the cross-track plane.

Using an LT-1 interferometric pair as a case study, a quantitative analysis is conducted, and the specific parameters for the selected LT-1 data are listed in Table 1. Figure 2 illustrates the correlation between terrain elevation and range pixel offset across varying perpendicular baselines. The results reveal two key observations: (1) For an interferometric pair with a 500 m perpendicular baseline, elevation variations of 0 to 1000 m generate a range pixel offset of 0 to 1.2 pixels. (2) When the perpendicular baseline increases to 2500 m, equivalent range-direction pixel offsets (0–1.2 pixels) occur with merely 0–200 m of elevation change. Furthermore, accounting for natural terrain undulation, longer baselines

significantly complicate the spatial distribution patterns of range-direction pixel offsets. However, this terrain-related range-direction offset cannot be accurately estimated using the conventional polynomial model (see Equation (8)). The co-registration results obtained with the conventional polynomial model are presented in the subsequent sections. Meanwhile, the method proposed by Sansosti et al. [26] was also adopted to estimate the range-direction offset. Due to errors in the interferometric geometric parameters, this method fails to achieve sub-pixel accuracy in range-direction offset estimation. For the sake of clarity, this approach is referred to as the "geometry-based method" in the following context, and its co-registration results are also demonstrated later in the paper. Subsequently, we simulated the range-direction offset using the actual LT-1 interferometric geometric parameters and corresponding DEM scenario according to Equation (5). As shown in Figure 3, the terrain-induced offset is non-negligible and poses challenges for high-precision co-registration.

Table 1. Parameters of the bistatic LT-1 interferometric pair.

Datasets	Range Pixel Spacing (m)	Look Angle (°)	Slant Range (m)	Critical Perpendicular Baseline (m)	Wavelength (cm)
LT-1	1.66	21.7	656,967	18,759	23.81

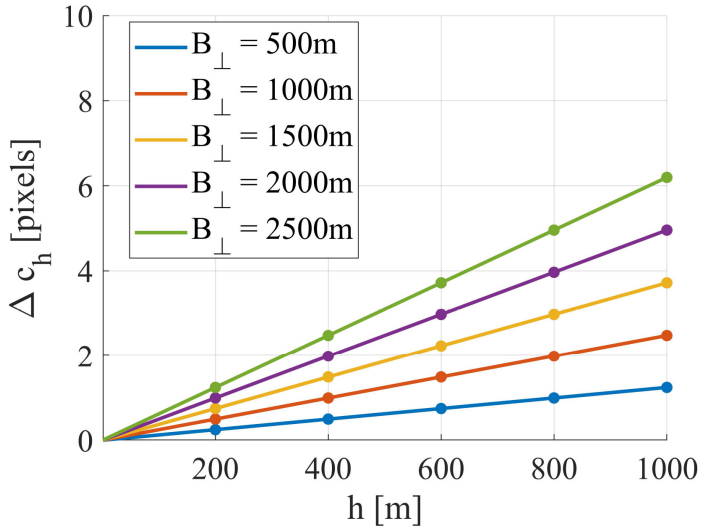


Figure 2. The relationship between terrain elevation (in meters) and range-direction offset (in pixels) at various perpendicular baseline lengths ($B_{\perp}$).

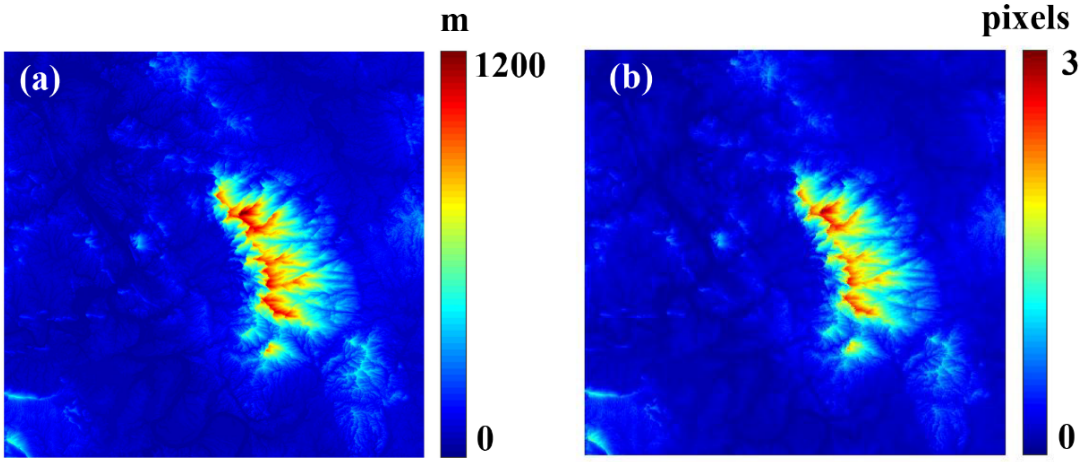


Figure 3. (**a**) Topography of the SAR scenario that was derived by the Copernicus DEM; (**b**) simulated range-direction offset.

3. Methodology

3.1. Enhanced SAR Images Co-Registration Model

Michel et al. [27] concluded that the pixel offset between the reference and secondary SAR images can be factorized as

$$off_{total} = off_{orb} + off_{topo} + off_{def} + off_{noi} \tag{6}$$

where the terms on the right-hand side of Equation (6) describe offset due to satellite orbit (off_{orb}) and topographic attitude $\left(off_{topo}\right)$, ground surface deformation $\left(off_{def}\right)$, and noise (off_{noi}). A single-pass (or bistatic) InSAR pair, such as the LT-1 mission, is acquired by one satellite transmitting radar pulses while both satellites simultaneously receive the radar echoes from the illuminated targets. Therefore, the pixel offsets caused by deformation and noise are not considered in our study, and Equation (6) can be rewritten as

$$off_{total} = off_{orb} + off_{topo} \tag{7}$$

For short-baseline interferometric pairs, the pixel offsets induced by topographic effects can be considered relatively small, with the offsets primarily caused by the satellite orbit. In this case, the offsets can be approximated by the following polynomial models:

$$\begin{cases} off^{r}_{total} \approx off^{r}_{orb} = \sum\limits_{j=0}^{N}\sum\limits_{k=0}^{j} a_{jk}x^{k}y^{j-k} \\ off^{az}_{total} \approx off^{az}_{orb} = \sum\limits_{j=0}^{N}\sum\limits_{k=0}^{j} b_{jk}x^{k}y^{j-k} \end{cases} \tag{8}$$

where the superscripts r and az denote the range and azimuthal directions. N is the polynomial degree, a_{jk} and b_{jk} are the unknown model parameters, and (x, y) are the image coordinates in SAR geometry. However, as elucidated in Section 2 and Equation (5), the slant-range pixel offset induced by terrain is linearly related to both the perpendicular baseline and terrain elevation. Therefore, for interferometric pairs with long baselines, this offset should be taken into account during fine co-registration. To achieve this goal, this study proposes an improved transformation model by incorporating an elevation term into the conventional polynomial model (see Equation (8)):

$$\begin{cases} off^{r}_{total} = off^{r}_{orb} + off^{r}_{topo} = \sum\limits_{j=0}^{N}\sum\limits_{k=0}^{j} a_{jk}x^{k}y^{j-k} + q{\cdot}h \\ off^{az}_{total} = off^{az}_{orb} + off^{az}_{topo} = \sum\limits_{j=0}^{N}\sum\limits_{k=0}^{j} b_{jk}x^{k}y^{j-k} \end{cases} \tag{9}$$

where q is the coefficient of the elevation term, h, which can be obtained from an external public DEM. For the azimuth direction, the conventional polynomial model is still adopted for co-registration. As elaborated earlier, the LT-1 data employs zero-Doppler imaging, and its flight tracks are nearly parallel. Therefore, the terrain-induced azimuthal offset can be neglected.

3.2. Parameter Determination

In the previous section, we proposed an improved transformation model, hereafter referred to as the DEM-based transformation model. In practical applications, a quadratic polynomial is commonly employed to estimate the offsets. To determine the unknown parameters in Equation (9), a minimum of seven valid observations is theoretically sufficient for computation. However, in reality, the number of available observations far exceeds this

requirement. Nevertheless, the presence of errors or even outliers in the observational data participating in the solution may adversely affect the model estimation. To address this issue, a robust least-squares estimation method is adopted [28]:

$$\hat{X} = \left(B^T P B\right)^{-1}\left(B^T P L\right) \tag{10}$$

where

$$L = \begin{bmatrix} off_1^r \\ \vdots \\ off_N^r \end{bmatrix} \quad B = \begin{bmatrix} 1 & y_1 & x_1 & y_1^2 & x_1 * y_1 & x_1^2 & h_1 \\ \vdots & \vdots & \vdots & \vdots & \vdots & \vdots & \vdots \\ 1 & y_N & x_N & y_N^2 & x_N * y_N & x_N^2 & h_N \end{bmatrix}$$

$$\hat{X} = \begin{bmatrix} a_{00} & a_{10} & a_{11} & a_{20} & a_{21} & a_{22} & q \end{bmatrix}^T$$

the superscript T represents the transpose matrix, and P denotes an $n \times n$ diagonal weight matrix. Subsequently, the IGG (Institute of Geodesy and Geophysics) method is adopted to solve Equation (10):

$$\alpha_i^b = \begin{cases} \frac{1}{\left|v_i^b\right| + \eta}, & \left|v_i^b\right| \le \sigma \\ \frac{1}{\left|v_i^b\right|}, & \sigma \le \left|v_i^b\right| \le 2\sigma \\ 0, & \left|v_i^b\right| > 2\sigma \end{cases} \qquad i = 1, 2, 3, \cdots, N;\ c = 1, 2, 3, \cdots \tag{11}$$

where $\sigma^2 = \left(\left(v^b\right)^T \cdot P^{b-1} \cdot v^b\right) / (\mathrm{N} - 1)$, c denotes the iteration count, v_i^c represents the observation residuals, and η is a minimal constant to prevent division by zero. The overall parameter estimation procedure is as follows:

$$\begin{aligned} p_i^c &= p_i^{c-1} \alpha_i^{c-1} \\ P^c &= diag\left[p_1^c\ p_2^c\ \cdots\ p_N^c\right] \\ X^c &= \left(B^T P^c B\right)^{-1}\left(B^T P^c L\right) \\ V^c &= B X^c - L \end{aligned} \tag{12}$$

Through iterative computations, the parameter estimates can be obtained. The iteration termination criterion is $\left|X^{c+1} - X^c\right| < \varepsilon$, which is an empirical value set to 10^{-6} in this study.

3.3. InSAR DEM Generation Based on the New Method

To better understand the proposed method and validate its effectiveness in topography mapping, the specific workflow is illustrated in Figure 4, including three parts. Part 1 involves geocoding the external DEM into the radar coordinate system, based on the orbital parameters and intensity of the reference SAR image. Part 2 first extracts homonymous points via the intensity cross-correlation algorithm, constructs the DEM-based transformation model, and then solves the model parameters using the robust least-squares method to achieve precise co-registration between the reference and secondary images. Subsequently, we resample the secondary image to the geometry of the reference SAR image according to the established transformation model. Part 3 applies the conventional InSAR processing methods to retrieve the InSAR DEM, which is then used to assess the effectiveness of the proposed method and to quantitatively evaluate the accuracy of topographic mapping using the bistatic LT-1 InSAR data.

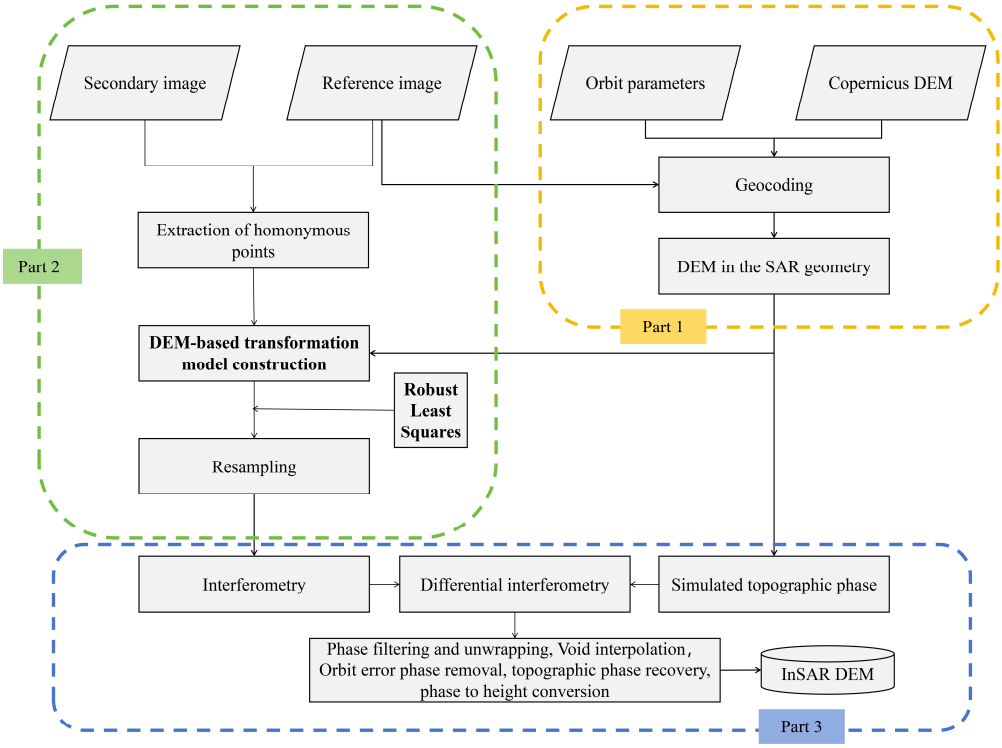


Figure 4. Flow chart of the proposed method for fine co-registration and DEM generation.

4. Study Areas and Datasets

4.1. Study Area

To validate the performance and effectiveness of our proposed approach, two study areas (see Figure 5), characterized by different terrain conditions and forest coverages, were selected. The first study area (3°35′23″~4°22′33″W, 40°32′33″~41°09′07″N) is located at the boundary between the Madrid Autonomous Community and Valladolid, Spain, as shown in Figure 5c. The central region features a mountain range with dense vegetation cover, while the surrounding areas consist of plains with sparse vegetation. The terrain in this study area is relatively simple, with the mountain range in the central region rising to elevations exceeding 2000 m, while the flat surrounding areas have elevations concentrated around 1000 m. The second study area (91°46′12″~92°27′17″E, 28°54′53″~29°30′53″N), shown in Figure 5d, is located in Shannan city, China. Compared to the first study area, this region is a rugged plateau marked by numerous gullies and consists primarily of bare land. Additionally, the terrain condition is quite complex, with elevations ranging from 3500 to 5700 m, and dramatic elevation changes relatively. Figure 6 displays the 30 m resolution DEM of the two selected study areas acquired by the Copernicus DEM.

4.2. SAR Data

The parameters of the LT-1 InSAR data employed in this study are listed in Table 2, while the red rectangles in Figure 5 correspond to the coverage of the LT-1 InSAR images. Both images were requested in Stripmap single-polarization mode (HH), with a chirp bandwidth of 80 MHz, and were provided with a pixel spacing of approximately 2.10 m. The two selected LT-1 images were used to constitute interferograms with vertical baselines of −1352 m and −2489 m, respectively.

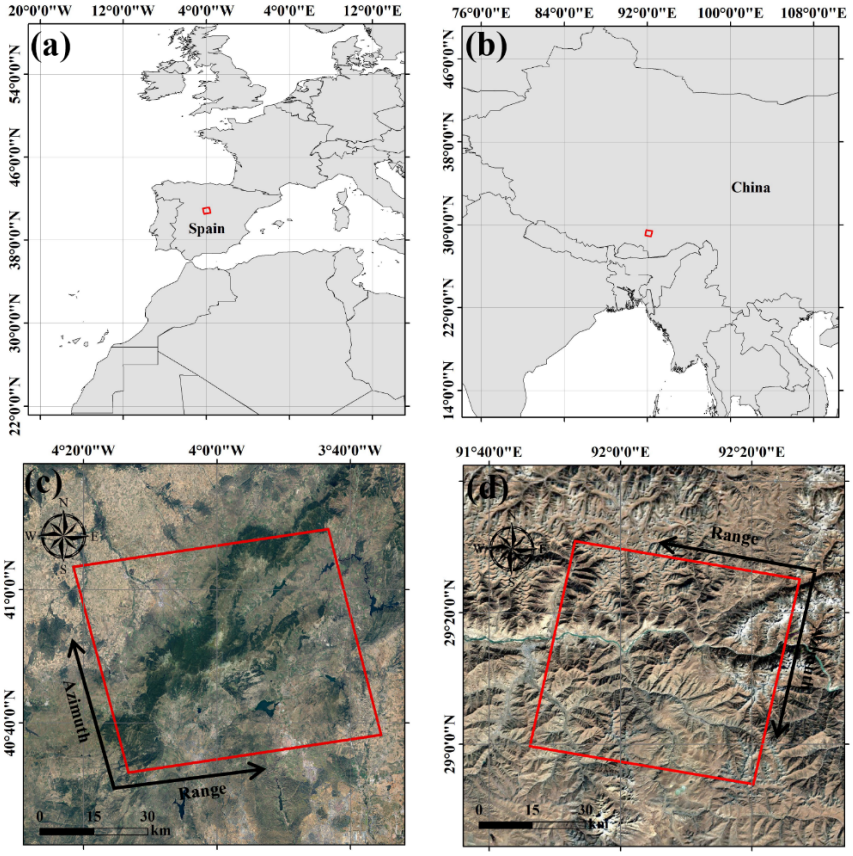


Figure 5. Geolocation of study areas: (**a**,**c**) Madrid, Spain, and (**b**,**d**) Shannan, China. The red rectangles indicate the coverage ranges of the LT-1 SAR images.

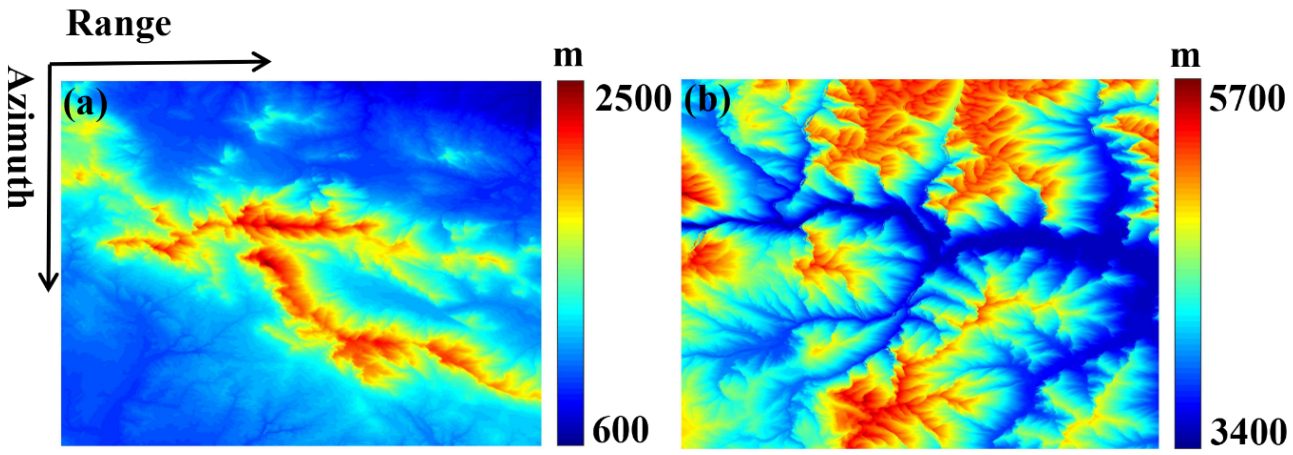


Figure 6. Topographic map in SAR coordinate system: (**a**) Madrid, Spain, and (**b**) Shannan, China.

Table 2. Summary of LT-1 SAR datasets employed in this study.

Study Area	Sensor	Acquisitions Date	Radar Look Angle (°)	Pixel Spacing (Range/Azimuth) (m)	Effective Baseline (m)
Madrid, Spain	LT-1A LT-1B	23 October 2022	26.31 26.11	1.67/2.13	−1352
Shannan, China	LT-1A LT-1B	26 October 2022	25.43 25.59	1.67/2.10	−2489

4.3. Reference DEM

NASADEM (NASA Digital Elevation Model) is an enhanced global elevation dataset developed as the successor to the Shuttle Radar Topography Mission (SRTM) DEM [29]. It was generated by reprocessing original SRTM radar data using improved interferometric unwrapping algorithms, which significantly reduced artifacts such as offsets and ramps in overlapping acquisition strips [30]. Vertical accuracy was refined through the integration of ICESat/GLAS-derived ground control points (GCPs), enabling precise height error corrections and tilt adjustments [31]. To minimize data voids, supplementary datasets including ASTER GDEM were incorporated, with remaining gaps predominantly filled by ASTER GDEM v3 [32]. Void-filled areas were masked to prevent inconsistencies between radar and optical-based elevation sources [33].

NASADEM provides near-global coverage at 1-arcsecond (~30 m) resolution with minimal voids, demonstrating superior accuracy and robustness compared to other open-access DEMs [34]. The dataset is distributed as $1^\circ \times 1^\circ$ tiles in WGS84 geographic coordinates, referenced to the Earth Gravistic Model 1996 (EGM96) geoid. As the most refined SRTM-derived elevation product, NASADEM serves as a critical resource for geospatial analysis, glaciology, and environmental monitoring.

5. Results

5.1. Madrid Test Site

Based on the proposed co-registration workflow, we first conducted SAR image co-registration and interferometry processing. Figure 7a–f show the associated interferogram and coherence maps. To assess the performance of the proposed method, we compared the proposed method with the conventional polynomial method and the geometry-based method [26]. Overall, all three methods produce similar interferometric fringes. From the coherence maps shown in Figure 7d–f, it is obvious that all three methods exhibit relatively high coherence in flat regions. However, in mountainous areas, our method effectively enhanced the co-registration accuracy, and the associated coherence is significantly improved and higher than that of the other two methods. Additionally, a more detailed quantitative evaluation of the three co-registration methods was conducted in a statistical mode. The evaluation of coherence across various methods is summarized in Table 3. The results indicate that the proposed method achieved a higher average coherence (approximately 0.04 higher, i.e., 0.75 vs. 0.79) than the other two methods, along with a smaller standard deviation (STD) and a lower void ratio (considering coherence values below 0.3 as invalid pixels).

Table 3. Summary of the coherence metrics at both test sites.

		Conventional Polynomial Model	Geometry-Based Method	Proposed Method
Madrid test site	Mean	0.75	0.75	0.79
	Standard Deviation	0.18	0.17	0.16
	Pixel ratio with coherence less than 0.3 (%)	5.30	4.70	4.20
Shannan test site	Mean	0.33	0.32	0.48
	Standard Deviation	0.21	0.22	0.25
	Pixel ratio with coherence less than 0.3 (%)	52.9	56.1	31.2

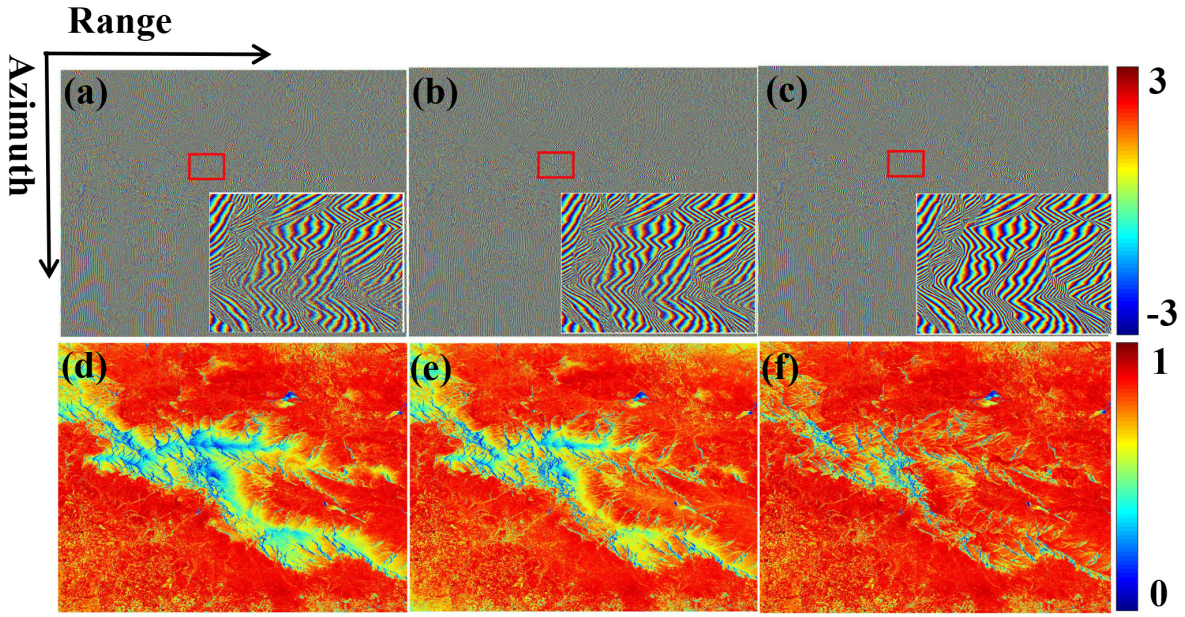


Figure 7. Madrid test site: interferometric quality evaluation. (**a**–**c**) Interference fringe images derived by conventional polynomial model, geometry−based method, and our proposed method; (**d**–**f**) the associated coherence maps. The sub-images presented in (**a**–**c**) indicate the enlarged images of the red rectangles in (**a**–**c**).

Finally, to quantitatively evaluate the effectiveness of the proposed method, the interferometric phases shown in Figure 7 were used to derive InSAR DEMs. Figure 8a–c show the InSAR DEMs derived from the interferometric phases of three co-registration methods. The associated elevation error maps with respect to the NASADEM are shown in Figure 8d–f. Overall, all three methods yield comparable results, but the conventional methods exhibit higher void ratios, which indicates the pixels with a coherence value below 0.3. In contrast, our proposed approach improves co-registration accuracy by incorporating terrain elevation data during the fine co-registration, so the decreased void ratio can be observed. Meanwhile, a quantitative comparison between the radar-based DEMs and the NASADEM was conducted, and two error measures were computed (see Table 4), namely the bias (corresponding to the mean error) and root mean square error (RMSE). The InSAR DEM derived by the proposed method achieves a lower RMSE of 2.87 m, outperforming both the conventional polynomial model (RMSE = 2.92 m) and the geometry-based method (RMSE = 2.89 m).

Table 4. Summary of the accuracy for various InSAR-based DEMs.

		Conventional Polynomial Model	Geometry-Based Method	Proposed Method
Madrid test site	Mean (m)	0.04	−0.02	−0.02
	RMSE (m)	2.92	2.89	2.87
Shannan test site	Mean (m)	0.26	0.05	0.15
	RMSE (m)	8.12	8.23	6.31

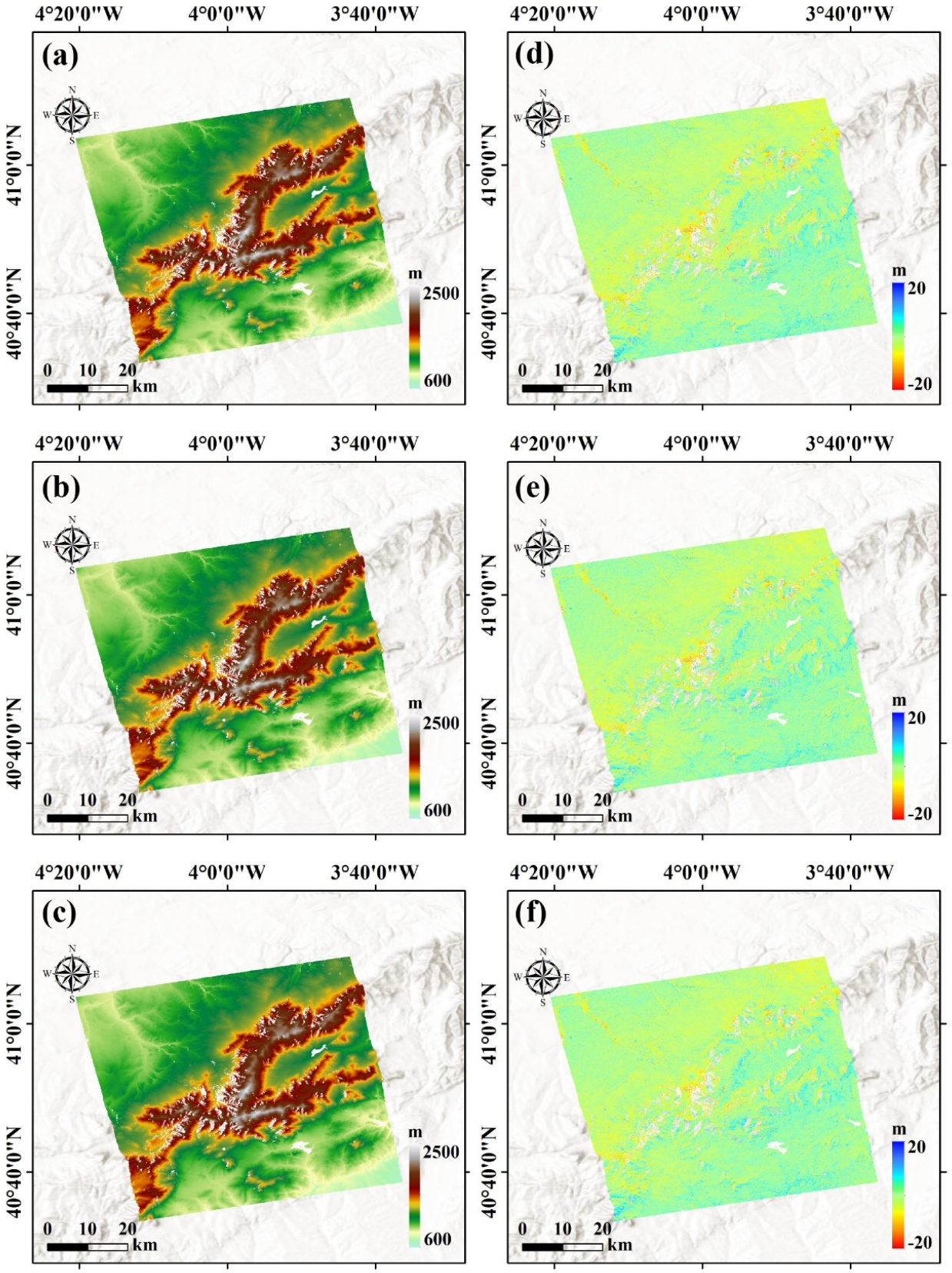


Figure 8. Madrid test site: topography evaluation. (**a**–**c**) InSAR DEM derived by conventional polynomial model, geometry−based method, and our proposed method; (**d**–**f**) the associated elevation error maps with respect to the NASADEM. The void areas correspond to the pixels with lower coherence.

5.2. Shannan Test Site

Similarly, the performance of the proposed method was evaluated at the Shannan test site. Figure 9a–c present interferograms generated by the three methods, demonstrating that the proposed method maintains clear and continuous interference fringes, while the other two methods exhibit poor fringe patterns. The coherence maps shown in Figure 9d–f reveal that the proposed method significantly improves low-coherence areas, elevating coherence values above 0.3 in regions where the other methods show extensive low-coherence zones. Furthermore, the coherence evaluation results are summarized in Table 3. The results indicate that compared with the reference methods, the proposed method achieves (1) higher average coherence (approximately 0.16 higher, i.e., 0.48 vs. 0.32) and (2) a lower percentage of low-quality pixels (31.2% vs. 56.1%).

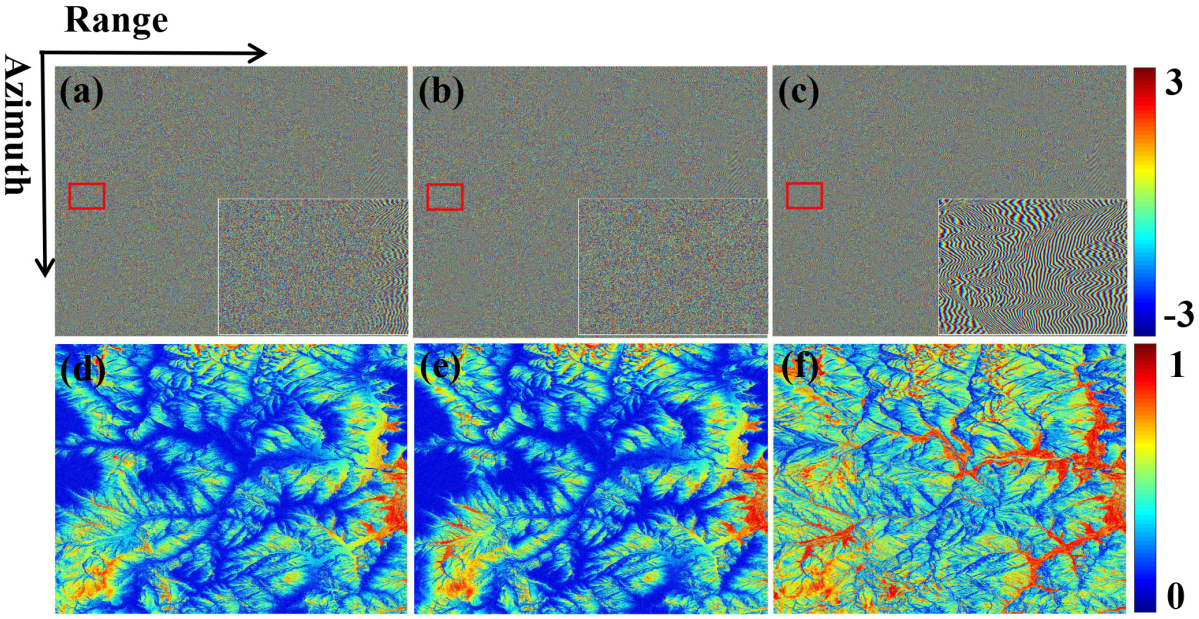


Figure 9. Shannan test site: interferometric quality evaluation. (**a**–**c**) Interference fringe images derived by conventional polynomial model, geometry−based method, and our proposed method; (**d**–**f**) the associated coherence maps. The sub-images in (**a**–**c**) indicate the enlarged images of the red rectangles in (**a**–**c**).

Finally, Figure 10a–c display the InSAR DEMs derived by the unwrapped phase using the three co-registration approaches, with their corresponding elevation error distributions relative to NASADEM shown in Figure 10d–f. Comparative analysis shows that both the conventional polynomial model and geometry-based method produce numerous elevation outliers, whereas the proposed method substantially reduces such anomalies. Notably, the InSAR DEM generated by our method achieves a lower RMSE of 6.31 m (see Table 4), outperforming both the traditional polynomial model (RMSE = 8.12 m) and the geometry-based approach (RMSE = 8.23 m).

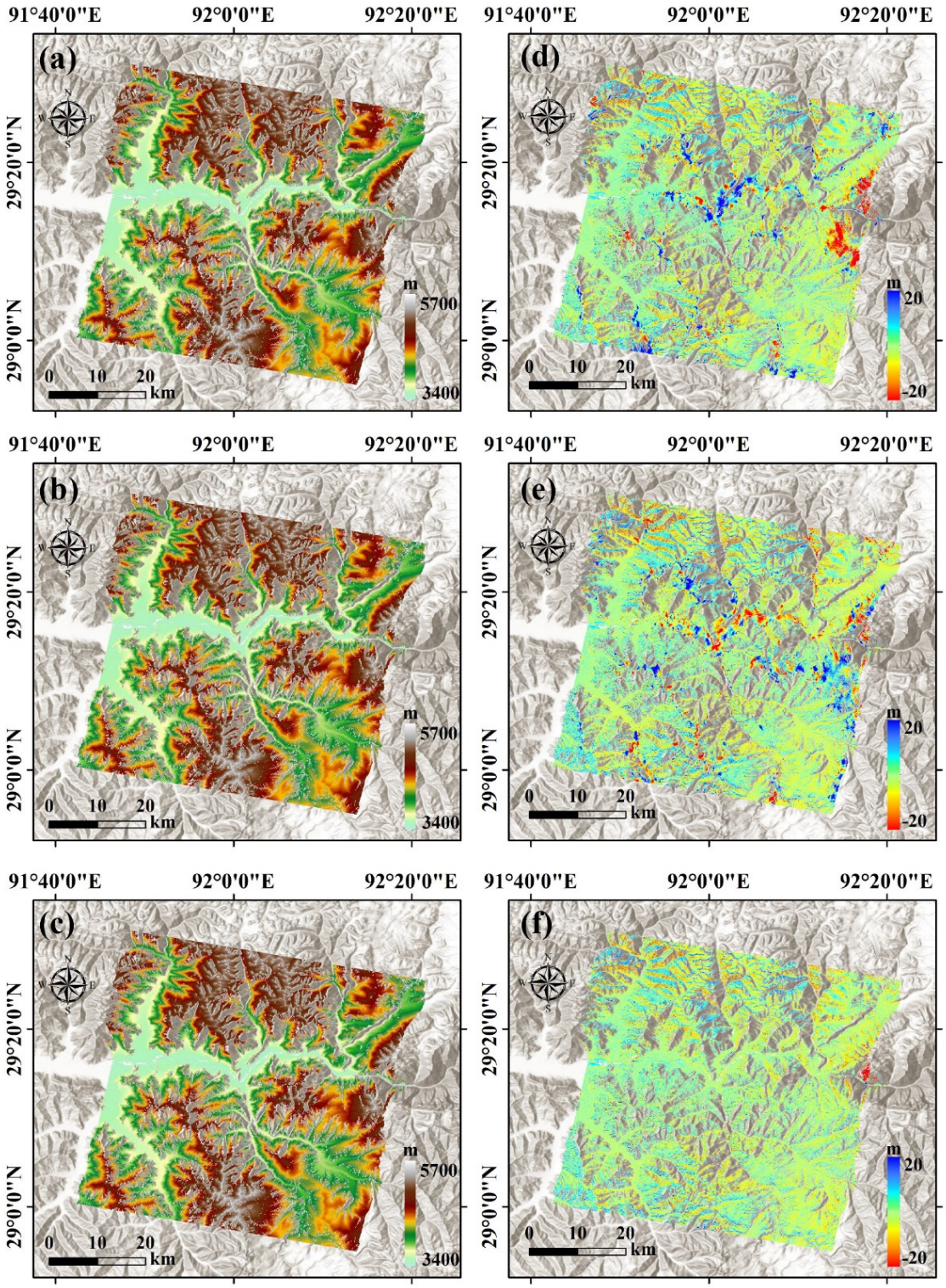


Figure 10. Shannan test site: topography evaluation. (**a**–**c**) InSAR DEM derived by conventional polynomial model, geometry−based method, and our proposed method; (**d**–**f**) the associated elevation error maps with respect to the NASADEM. The void areas correspond to the pixels with lower coherence.

6. Discussion

6.1. Topographic Influence Mechanisms in SAR Fine Co-Registration

As elucidated in Section 2, the offsets induced by terrain are not negligible during fine co-registration. To further demonstrate its effects, Figure 11 presents scatterplots of

the range-direction offset residuals (representing the difference between estimated and referenced offsets) against relative elevation (indicating the deviation from the scene's mean elevation). The conventional polynomial model yields offset residuals that follow a linear trend with respect to relative elevation (see Figure 11a,d), with residuals exceeding 1 pixel near ridges and valleys. This leads to significant coherence loss in these areas (see Figures 7d and 9d). Similarly, the geometry-based method also exhibits a linear distribution of offset residuals (see Figure 11b,e), which can be attributed to the inaccuracies in satellite orbital records and deviations in relative positioning. Conversely, the proposed method produces residuals that do not show a linear dependence on relative elevation (see Figure 11c,f) but rather are randomly distributed around zero. In the proposed method, the coefficient preceding the elevation term h is 0.001146 for the Madrid test site and 0.0023 for the Shannan test site. This demonstrates that the proposed method can effectively characterize the offset induced by terrain elevation: the elevation-derived offset at the Shannan site is approximately twice that at the Madrid site, which is highly consistent with the actual range-direction offset residual map presented in Figure 11. Therefore, our proposed method yields improved interferometric quality and significantly higher coherence.

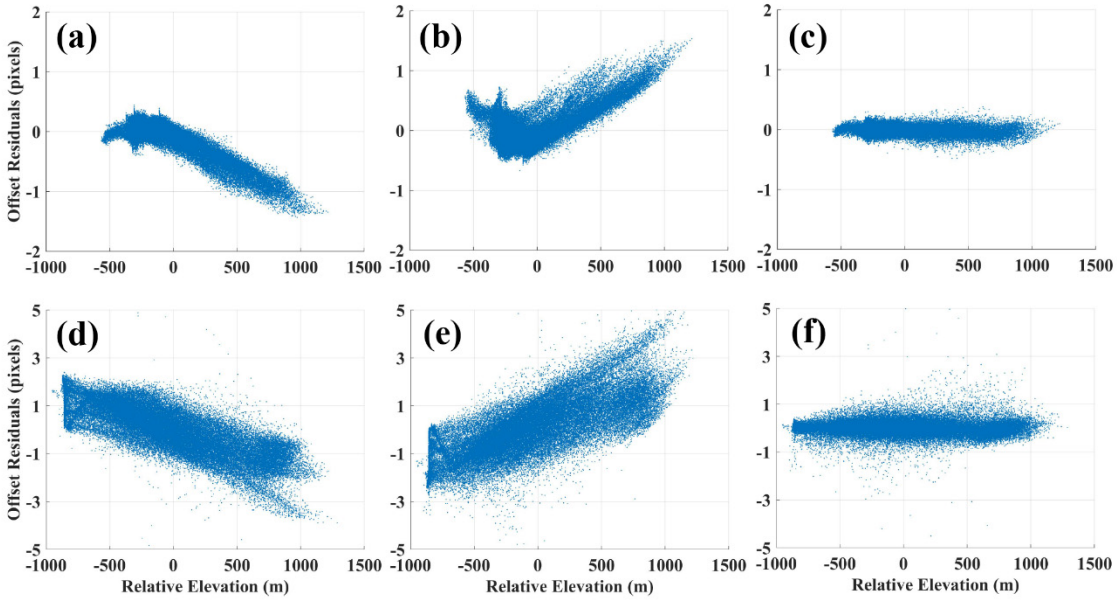


Figure 11. Madrid test site: scatterplots of the relative elevation versus range−direction offset residuals. (**a**) Conventional polynomial model, (**b**) geometry−based method, and (**c**) proposed method. Shannan test site: (**d**) conventional polynomial model, (**e**) geometry−based method, and (**f**) proposed method.

6.2. Impact of External DEM on the Proposed Method

Since the proposed fine co-registration method requires an external DEM, it is essential to analyze its effect on the effectiveness. To achieve this goal, three DEMs, characterized by different resolutions, were tested, including Copernicus DEM with 30 m resolution and SRTM DEM with 30 m and 90 m resolutions. A comparative analysis was conducted in the Shannan study area, which has a highly fragmented and undulating mountain topography (Figure 12). The results indicate that coherence discrepancies remain below 0.05 when employing different multi-looking parameter combinations (1×1 vs. 5×2) or alternative DEM sources. The results demonstrate that the proposed method exhibits low dependence on external DEM precision, thereby verifying that contemporary, freely accessible open-source DEM products adequately fulfill co-registration requirements. However, it should be noted that while the proposed method does not require extremely high-precision external DEMs, it still relies on a reasonably accurate external DEM to support the co-registration

process. How to achieve high-precision co-registration in scenarios without external DEMs warrants further investigation. Additionally, with the development of SAR technology, an increasing number of high-resolution (even centimeter-level) SAR products are emerging. Whether the existing publicly available free 30 m resolution external DEMs can meet the requirements of this algorithm deserves further consideration—for centimeter-level resolution SAR images, geocoding alone may pose a significant challenge.

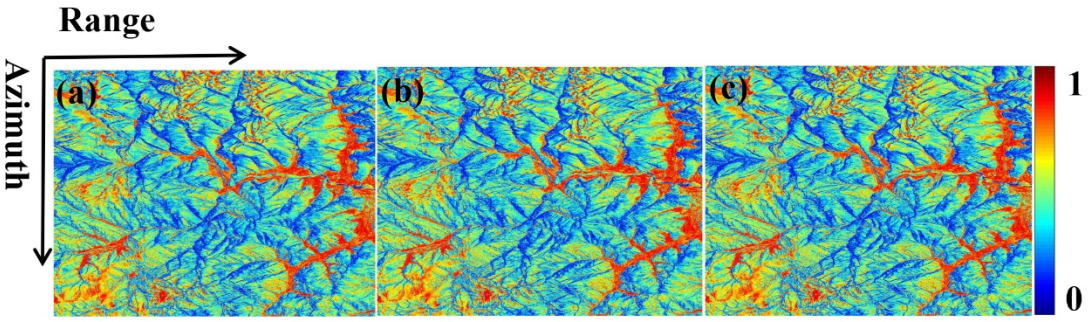


Figure 12. Spatial distribution of coherence when different DEMs were used: (**a**) Copernicus DEM at 30 m resolution, (**b**) SRTM 30 DEM, and (**c**) SRTM 90 DEM.

6.3. Effects of Different Terrain Conditions on InSAR DEM Generation

In the Madrid test site, to analyze the correlation between topographic conditions and DEM elevation error, the DEM errors were divided into five groups according to the relative elevations. Figure 13 shows both the RMSE values of InSAR-based DEMs (with respect to the NASA reference DEM) and the corresponding coherence statistics for each elevation group. Overall, across all three co-registration methods, RMSE values show a consistent increasing trend as the relative height increases, reflecting progressive degradation in DEM inversion accuracy. Conversely, mean coherence values demonstrate an inverse relationship with relative elevation.

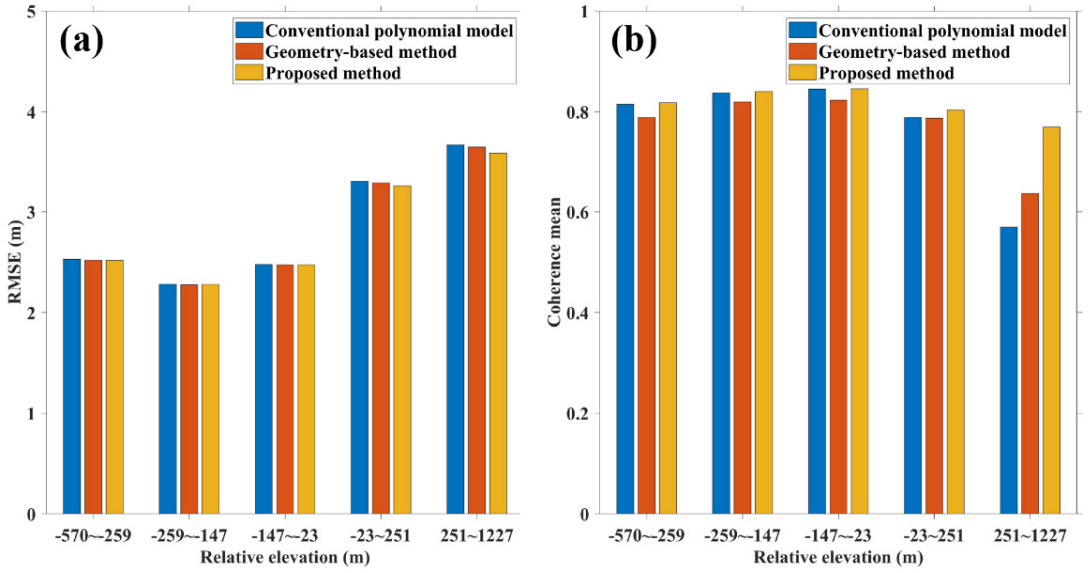


Figure 13. Madrid test site: statistical histograms of evaluation metrics for different relative elevation intervals. (**a**) RMSE of InSAR DEM and (**b**) average coherence.

Additionally, all three methods demonstrate comparable topographic measurement performance when the relative height is below 251 m, though the proposed method maintains slightly higher average coherence. In areas where the relative terrain height exceeds 251 m, the proposed method shows significantly improved performance—achieving both

higher mean coherence (0.77) and lower RMSE (3.59 m) values compared to the conventional polynomial model and geometry-based method. These results confirm that the proposed method maintains superior performance across all elevation groups, particularly in high-relief terrain.

At the Shannan test site (characterized by rugged terrain), Figure 14a reveals that the proposed method generates DEMs with consistently lower RMSE values across all relative elevation groups, showing 22.3% and 23.3% greater accuracy than the conventional polynomial and geometry-based methods, respectively. Meanwhile, the conventional methods exhibit distinct topographically dependent error patterns: their RMSE values follow a characteristic U-shaped distribution relative to the relative elevation. This pattern indicates significantly larger errors in high-relief zones where geometric distortions are most pronounced. In contrast, the proposed method's flatter error distribution demonstrates its robustness across varying terrain conditions.

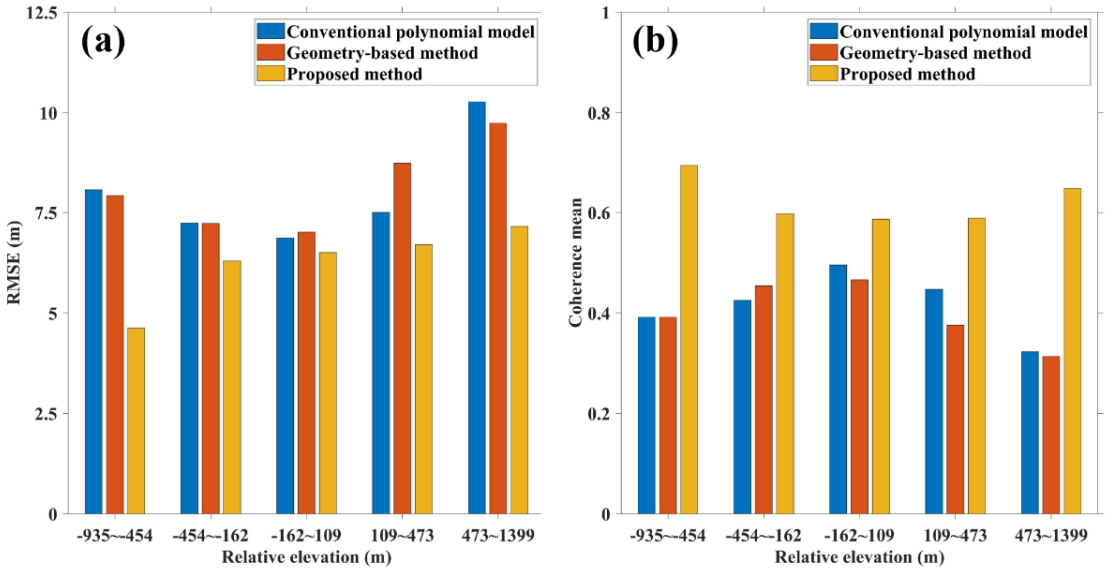


Figure 14. Shannan test site: statistical histograms of evaluation metrics for different relative elevation intervals. (**a**) RMSE of InSAR DEM and (**b**) average coherence.

Regarding the mean coherence, Figure 14b demonstrates that the proposed method consistently achieves higher coherence values compared to conventional approaches. Notably, it demonstrates superior stability in both valley and ridge regions, with particularly marked improvements under rugged terrain conditions.

7. Conclusions

This paper presented an enhanced fine co-registration transformation model for long-baseline SAR image pairs, which incorporates terrain elevation to compensate for the pixel offsets induced by terrain. The proposed method was evaluated using bistatic LT-1 SAR data collected at various terrain conditions and baseline configurations. Comparative analyses against the conventional polynomial model and geometry-based method demonstrated the performance of the proposed method through two key metrics: (1) interferometric quality assessed via coherence maps and (2) DEM accuracy verified against NASADEM. The results show that our proposed model significantly improves co-registration precision, particularly in complex-terrain environments. These results provide a robust SAR image co-registration framework for retrieving higher-accuracy DEMs from LT-1 data. Furthermore, this study provides technical guarantees for future SAR missions requiring precise co-registration under complex topographic conditions.

Author Contributions: Conceptualization, H.F.; methodology, D.Z.; software, M.Z.; validation, K.W.; formal analysis, D.Z. and Z.L. (Zhiwei Liu); investigation, D.Z.; resources, Q.H.; data curation, Z.L. (Zhiwei Li); writing—original draft preparation, D.Z.; writing—review and editing, D.Z., H.F. and Z.L. (Zhiwei Liu); visualization, D.Z.; supervision, A.W.; project administration, J.Z.; funding acquisition, J.Z. All authors have read and agreed to the published version of the manuscript.

Funding: This work was funded by the National Natural Science Foundation of China (Nos. 42227801, 42330112), the Natural Science Foundation for Excellent Young Scholars of Hunan Province (No. 2023JJ20061), and in part by the National Key R&D Program of China (No. 2022YFB3902605).

Data Availability Statement: The data supporting the findings of this study were provided by the China Center for Resources Satellite Data and Application (their support is acknowledged separately). Researchers requiring access to the data for academic research must follow the official data application procedures of the China Centre for Resources Satellite Data and Application. Detailed access guidelines and requirements are available on the center's official website or via direct contact with the center. The corresponding author may provide assistance in clarifying the application process if necessary.

Acknowledgments: We would like to thank the China Center for Resources Satellite Data and Application for providing data support for this experiment.

Conflicts of Interest: The authors declare no conflicts of interest.

References

1. Mustieles-Perez, V.; Kim, S.; Krieger, G.; Villano, M. New Insights Into Wideband Synthetic Aperture Radar Interferometry. *IEEE Geosci. Remote Sens. Lett.* **2024**, *21*, 1–5. [CrossRef]
2. Bernhard, P.; Haener, D.; Frey, O. Detection of Railway Track Anomalies Using Interferometric Time Series of TerraSAR-X Satellite Radar Data. *IEEE J. Sel. Top. Appl. Earth Obs. Remote Sens.* **2024**, *17*, 11750–11760. [CrossRef]
3. Xue, F.; Wang, J.; Zheng, M.; Zhang, H.; Liu, X.; Wang, L.; Jia, X.; Deng, Y. Dual-Frequency Four-Stage Polarimetric SAR Interferometry for Forest Height Estimation. *IEEE Trans. Geosci. Remote Sens.* **2024**, *62*, 1–15. [CrossRef]
4. Delgado, F.; Shreve, T.; Borgstrom, S.; León-Ibáñez, P.; Castillo, J.; Poland, M. A Global Assessment of SAOCOM-1 L-Band Stripmap Data for InSAR Characterization of Volcanic, Tectonic, Cryospheric, and Anthropogenic Deformation. *IEEE Trans. Geosci. Remote Sens.* **2024**, *62*, 1–21. [CrossRef]
5. Mao, Q.; Li, Y.; Zhu, Y. A Hierarchical Feature Fusion and Attention Network for Automatic Ship Detection From SAR Images. *IEEE J. Sel. Top. Appl. Earth Obs. Remote Sens.* **2024**, *17*, 13981–13994. [CrossRef]
6. Xu, X.; Sandwell, D.T.; Tymofyeyeva, E.; González-Ortega, A.; Tong, X. Tectonic and Anthropogenic Deformation at the Cerro Prieto Geothermal Step-Over Revealed by Sentinel-1A InSAR. *IEEE Trans. Geosci. Remote Sens.* **2017**, *55*, 5284–5292. [CrossRef]
7. Alcantarilla, P.F.; Bartoli, A.; Davison, A.J. KAZE Features. In Proceedings of the Computer Vision–ECCV 2012: 12th European Conference on Computer Vision, Florence, Italy, 7–13 October 2012; Springer: Berlin/Heidelberg, Germany, 2012; pp. 214–227.
8. Bay, H.; Ess, A.; Tuytelaars, T.; Van Gool, L. Speeded-up Robust Features (SURF). *Comput. Vis. Image Underst.* **2008**, *110*, 346–359. [CrossRef]
9. Schwind, P.; Suri, S.; Reinartz, P.; Siebert, A. Applicability of the SIFT Operator to Geometric SAR Image Registration. *Int. J. Remote Sens.* **2010**, *31*, 1959–1980. [CrossRef]
10. Dellinger, F.; Delon, J.; Gousseau, Y.; Michel, J.; Tupin, F. SAR-SIFT: A SIFT-like Algorithm for SAR Images. *IEEE Trans. Geosci. Remote Sens.* **2014**, *53*, 453–466. [CrossRef]
11. Manduchi, R.; Mian, G.A. Accuracy Analysis for Correlation-Based Image Registration Algorithms. In Proceedings of the 1993 IEEE International Symposium on Circuits and Systems, Chicago, IL, USA, 3–6 May 1993; Volume 1, pp. 834–837.
12. Maes, F.; Collignon, A.; Vandermeulen, D.; Marchal, G.; Suetens, P. Multimodality Image Registration by Maximization of Mutual Information. *IEEE Trans. Med. Imaging* **1997**, *16*, 187–198. [CrossRef]
13. Homer, J.; Longstaff, I. Minimising the Tie Patch Window Size for SAR Image Co-Registration. *Electron. Lett.* **2003**, *39*, 122–124. [CrossRef]
14. Shi, X.; Zhang, Y.; Jiang, J. InSAR Image Registration Using Modified Correlation Coefficient Algorithm. In Proceedings of the 2006 7th International Symposium on Antennas, Propagation & EM Theory, Guilin, China, 26–29 October 2006; pp. 1–4.
15. Li, D.; Zhang, Y. A Fast Offset Estimation Approach for InSAR Image Subpixel Registration. *IEEE Geosci. Remote Sens. Lett.* **2012**, *9*, 267–271. [CrossRef]

16. Pallotta, L.; Giunta, G.; Clemente, C. Subpixel SAR Image Registration Through Parabolic Interpolation of the 2-D Cross Correlation. *IEEE Trans. Geosci. Remote Sens.* **2020**, *58*, 4132–4144. [CrossRef]
17. Wegmuller, U.; Werner, C.; Strozzi, T. SAR Interferometric and Differential Interferometric Processing Chain. In Proceedings of the IGARSS '98. Sensing and Managing the Environment. 1998 IEEE International Geoscience and Remote Sensing. Symposium Proceedings. (Cat. No.98CH36174), Seattle, WA, USA, 6–10 July 1998; Volume 2, pp. 1106–1108.
18. Simonetto, E.; Follin, J.-M. An Overview on Interferometric SAR Software and a Comparison Between DORIS and SARSCAPE Packages. In *Geospatial Free and Open Source Software in the 21st Century*; Bocher, E., Neteler, M., Eds.; Springer: Berlin/Heidelberg, Germany, 2012; pp. 107–122, ISBN 978-3-642-10595-1.
19. Reigber, A.; Hellwich, O. RAT (Radar Tools): A Free SAR Image Analysis Software Package. In Proceedings of the EUSAR, Ulm, Germany, 25–27 May 2004; Volume 4, pp. 997–1000.
20. Nitti, D.O.; Hanssen, R.F.; Refice, A.; Bovenga, F.; Nutricato, R. Impact of DEM-Assisted Coregistration on High-Resolution SAR Interferometry. *IEEE Trans. Geosci. Remote Sens.* **2011**, *49*, 1127–1143. [CrossRef]
21. Yue, H.; Hanssen, R.; Kianicka, J.; Marinkovic, P.; Van Leijen, F.; Ketelaar, G. Sensitivity of Topography on InSAR Data Coregistration. In Proceedings of the ENVISAT & ERS Symposium, Salzburg, Austria, 6–10 September 2004; pp. 6–10.
22. She, J.; Tan, Y. Research on Runge Phenomenon. *Comput. Math. Biophys.* **2019**, *8*, 1500–1510.
23. Zhang, Z.; Liu, H.; Zhang, L.; Wang, S.; Li, Z.; Wu, J. A Large Width SAR Image Registration Method Based on the Compelex Correlation Function. In Proceedings of the 2016 IEEE International Geoscience and Remote Sensing Symposium (IGARSS), Beijing, China, 10–15 July 2016; pp. 6476–6479.
24. Cheng, L.; Wang, Y.; Li, M.; Zhong, L.; Wang, J. Generation of Pixel-Level SAR Image Time Series Using a Locally Adaptive Matching Technique. *Photogramm. Eng. Remote Sens.* **2014**, *80*, 839–848. [CrossRef]
25. Mou, J.; Wang, Y.; Hong, J.; Wang, Y.; Wang, A.; Sun, S.; Liu, G. First Assessment of Bistatic Geometric Calibration and Geolocation Accuracy of Innovative Spaceborne Synthetic Aperture Radar LuTan-1. *Remote Sens.* **2023**, *15*, 5280. [CrossRef]
26. Sansosti, E.; Berardino, P.; Manunta, M.; Serafino, F.; Fornaro, G. Geometrical SAR Image Registration. *IEEE Trans. Geosci. Remote Sens.* **2006**, *44*, 2861–2870. [CrossRef]
27. Michel, R.; Avouac, J.-P.; Taboury, J. Measuring near Field Coseismic Displacements from SAR Images: Application to the Landers Earthquake. *Geophys. Res. Lett.* **1999**, *26*, 3017–3020. [CrossRef]
28. Wang, H.; Zhu, J.; Fu, H.; Feng, G.; Wang, C. Modeling and Robust Estimation for the Residual Motion Error in Airborne SAR Interferometry. *IEEE Geosci. Remote Sens. Lett.* **2019**, *16*, 65–69. [CrossRef]
29. Fan, Y.; Ke, C.-Q.; Zhou, X.; Shen, X.; Yu, X.; Lhakpa, D. Glacier Mass-Balance Estimates over High Mountain Asia from 2000 to 2021 Based on ICESat-2 and NASADEM. *J. Glaciol.* **2023**, *69*, 500–512. [CrossRef]
30. Crippen, R.; Buckley, S.; Agram, P.; Belz, E.; Gurrola, E.; Hensley, S.; Kobrick, M.; Lavalle, M.; Martin, J.; Neumann, M.; et al. NASADEM Global Elevation Model: Methods and Progress. *Int. Arch. Photogramm. Remote Sens. Spat. Inf. Sci.* **2016**, *41*, 125–128. [CrossRef]
31. Chen, W.; Yao, T.; Zhang, G.; Li, F.; Zheng, G.; Zhou, Y.; Xu, F. Towards Ice Thickness Inversion: An Evaluation of Global DEMs by ICESat-2 in the Glacierized Tibetan Plateau. *Cryosphere Discuss.* **2021**, *16*, 197–218. [CrossRef]
32. Okolie, C.J.; Mills, J.P.; Adeleke, A.K.; Smit, J.L.; Peppa, M.V.; Altunel, A.O.; Arungwa, I.D. Assessment of the Global Copernicus, NASADEM, ASTER and AW3D Digital Elevation Models in Central and Southern Africa. *Geo-Spat. Inf. Sci.* **2024**, *27*, 1362–1390. [CrossRef]
33. Braun, M.H.; Malz, P.; Sommer, C.; Farías-Barahona, D.; Sauter, T.; Casassa, G.; Soruco, A.; Skvarca, P.; Seehaus, T.C. Constraining Glacier Elevation and Mass Changes in South America. *Nat. Clim. Change* **2019**, *9*, 130–136. [CrossRef]
34. Meadows, M.; Jones, S.; Reinke, K. Vertical Accuracy Assessment of Freely Available Global DEMs (FABDEM, Copernicus DEM, NASADEM, AW3D30 and SRTM) in Flood-Prone Environments. *Int. J. Digit. Earth* **2024**, *17*, 2308734. [CrossRef]

Disclaimer/Publisher's Note: The statements, opinions and data contained in all publications are solely those of the individual author(s) and contributor(s) and not of MDPI and/or the editor(s). MDPI and/or the editor(s) disclaim responsibility for any injury to people or property resulting from any ideas, methods, instructions or products referred to in the content.